Dalton Transactions

Computational investigation into intramolecular hydrogen bonding controlling the isomer formation and pK_a of octahedral nickel (II) proton reduction catalysts

Journal:	*Dalton Transactions*
Manuscript ID	DT-ART-01-2022-000043.R1
Article Type:	Paper
Date Submitted by the Author:	02-Feb-2022
Complete List of Authors:	Bhattacharjee, Avik; Portland State University, Chemistry Brown, Dayalis; Portland State University, Chemistry Virca, Carolyn; Portland State University, Chemistry Ethridge, Trent; Portland State University, Chemistry Mendez Galue, Oreana; Portland State University Pham, Uyen; Portland State University McCormick, T.; Portland State University, Chemistry

ARTICLE

Computational investigation into intramolecular hydrogen bonding controlling the isomer formation and pK_a of octahedral nickel (II) proton reduction catalysts

Received 00th January 20xx,
Accepted 00th January 20xx

DOI: 10.1039/x0xx00000x

Avik Bhattacharjee, Dayalis S.V. Brown, Carolyn N. Virca, Trent E. Ethridge, Oreana Mendez Galue, Uyen T. Pham and Theresa M. McCormick *

This work demonstrates the impact of intramolecular hydrogen bonding (H-bonding) on the calculated pK_a of octahedral tris-(pyridinethiolato)nickel (II), **[Ni(PyS)$_3$]$^-$**, proton reduction catalysts. Density Functional Theory (DFT) calculations on a **[Ni(PyS)$_3$]$^-$** catalyst, and eleven derivatives, demonstrate geometric isomer formation in the protonation step of the catalytic cycle. Through Quantum Theory of Atoms in Molecules (QTAIM), we show that the pK_a of each isomer is driven by intramolecular H-bonding of the proton on the pyridyl nitrogen to a sulfur on a neighboring ligand. This work demonstrates that ligand modification *via* the placement of electron-donating (ED) or electron-withdrawing (EW) groups may have unexpected effects on the catalyst's pK_a due to intramolecular H-bonding and isomers need to be considered in computational work. This work suggests the possibility that modification of substituent placement on the ligands to manipulate H-bonding in homogeneous metal catalysts could be explored as a tool to simultaneously target both desired pK_a and E^0 values in small molecule catalysts.

Introduction

Electrochemical and photochemical proton reduction catalysts that generate hydrogen from water have potential applications in storing solar energy through artificial photosynthesis.[1,2] The pK_a of such compounds can play a critical role in their reactivity and the conditions in which they operate. Proton reduction catalysts are characterized by the pH required for protonation of the catalyst, as well as the electrochemical potential (E^0), required for hydrogen production.[3–7] Understanding the structural factors that contribute to pK_a and E^0 is critical to predict structure-function relationships.[8–11] Computational studies allow for the detailed investigation of these two thermodynamic properties of the catalyst.[12,13] The extensive use of DFT has allowed for notable success in the field of catalyst design, ligand modification, and enhancement of catalytic efficiency, in particular for homogeneous metal catalysts, and thus has proven to be an indispensable tool.[14–20] However, it is imperative to acquire a thorough knowledge of the intricacies involved in a system through a judicious survey of the molecular model that can justify the mechanistic details of the catalytic cycle in order to obtain unambiguous results.

Homogeneous catalysts based on earth-abundant metals have been shown to be efficient in converting protons to hydrogen gas.[21–34] This work examines the computationally derived structures involved in the catalytic cycle for hydrogen production by

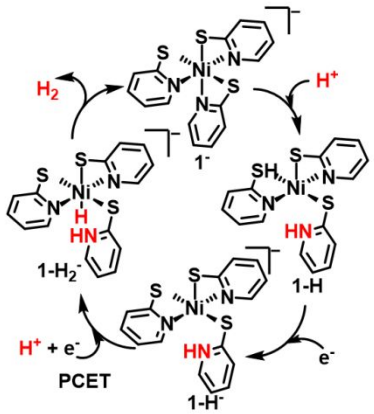

Figure 1. The proposed catalytic cycle of **[Ni(PyS)$_3$]$^-$** catalyst. Compound **1$^-$** is protonated at a pyridyl N to form **1-H**. This is then reduced to **1-H$^-$**. Subsequent addition of another proton and electron makes the intermediate **1-H$_2^-$** that can release H_2 to regenerate **1$^-$**.

tris-(pyridinethiolato)nickel (II), often reported as nickel (II) tris-(pyridinethiolate), **[Ni(PyS)$_3$]$^-$**, and its derivatives, originally developed by Eisenberg and co-workers.[22,33] The catalytic cycle has been proposed to proceed through a CECE (Chemical-Electrochemical-Chemical-Electrochemical) mechanism, starting with protonation of one of the pyridyl N atoms (**Figure 1**).[35] Both computational and X-ray studies have shown that the three pyridinethiolate (PyS$^-$) ligands are oriented in a pseudo-octahedral

Portland State University, College of Liberal Arts & Sciences, Department of Chemistry, Post Office Box 751 CHEM, Portland, Oregon 97207, USA.
E-mail: t.m.mccormick@pdx.edu
† Electronic Supplementary Information (ESI) available: Single point energies, Bond lengths, Topology maps and coordinates for all reported compounds in an .xyz file. See DOI: 10.1039/x0xx00000x

meridional geometry around the Ni(II) center.[33,35,36] The asymmetric chelation of bidentate PyS^- ligands results in each coordinated atom occupying a unique chemical environment. In this computational work, we show that protonation of each of the three pyridyl N atoms results in geometric isomers of the protonated intermediate with calculated pK_a values varying by up to ~3 pK_a units between the isomers for a single compound.

The formation of geometric isomers during the catalytic cycle of H_2 production by **[Ni(PyS)$_3$]$^-$** has not been considered previously. By separately modeling all possible isomers formed by the protonation of the starting **[Ni(PyS)$_3$]$^-$** catalyst, we are able to identify structural elements that significantly impact the calculated thermodynamic parameters of each geometric isomer. Specifically, we have found that intramolecular H-bonding plays a key role in the pK_a values of the different protonated isomers of the catalyst. H-bonding has a pivotal role in explaining the structure-function relationship in large macro-molecular systems like proteins.[37–40] However, large changes in the pK_a of small inorganic complexes due to intramolecular H-bonding have been relatively unexplored. Reports by Kass *et. al*, showed the importance of inter- and intra-molecular H-bonding on the pK_a of organic acids and their reactivity.[41,42] The effect of H-bonding on the transition metal catalysis has also been reported in experimental and computational studies where they found H-bonding can facilitate the catalytic pathways by stabilizing intermediates. For example, hydrogen evolution **[Ni(P$_2$N$_2$)$_2$]$^{2+}$** type catalysts shows an intramolecular Ni…H-N bonding during catalysis.[43] Another Ni(0) catalyst operates in reversible alkenyl functional group swapping reaction by the formation of catalytic intermediates stabilized by H-bonding interactions.[44] Intramolecular H-bonding, however rare, plays a crucial role in small molecule catalysis. Through computations, we have found the calculated structure of protonated **[Ni(PyS)$_3$]$^-$** catalyst is complicated by both isomer formation and intramolecular H-bonding. We have found that the lowest energy isomer formed during the protonation step of the catalytic cycle is controlled through the H-bond stabilization energy which overcomes the thermodynamic *trans* effect.

Ligand modification is often employed to improve catalytic turnover frequency and overpotential by tuning the pK_a and E^0.[22,36] We have found, through the modeling of several catalysts with ligand modification, that structural changes result in unique population distributions of the isomers for each catalyst, which do not directly correlate with the electronic effects of the substituents. This work explores the role of intramolecular H-bonding on the structure and stability of the catalytic intermediates of the proton reduction catalyst, **[Ni(L1)$_3$]$^-$** and six derivatives (**[Ni(L2)$_3$]$^-$** through **[Ni(L7)$_3$]$^-$**) using computational methodologies and compared to experimental results (**Scheme 1**). The knowledge gathered from those compounds were further employed to five other derivatives with ligands that are not commercially available (**[Ni(L8)$_3$]$^-$** through **[Ni(L12)$_3$]$^-$**) using computational modeling (**Scheme 1**). The comparison to experimental data highlights the necessity of computationally considering the structural isomers to provide an explanation for unanticipated results. We have calculated pK_a, E^0 values, and the Boltzmann population distribution of the geometric isomers of each catalyst based on computed thermodynamic energies. Topological analyses further revealed that the varying stability of these isomers results from the strength of the intramolecular H-bond between the H attached to the pyridyl N and the S atom from an adjacent PyS^- ligand. The structure-reactivity relationship uncovered herein highlights the importance of carefully considering geometric isomers while conducting computational studies on octahedral complexes. This report aims to benefit chemists studying the catalytic mechanism of octahedral metal-ligand complexes to understand their system in greater detail.

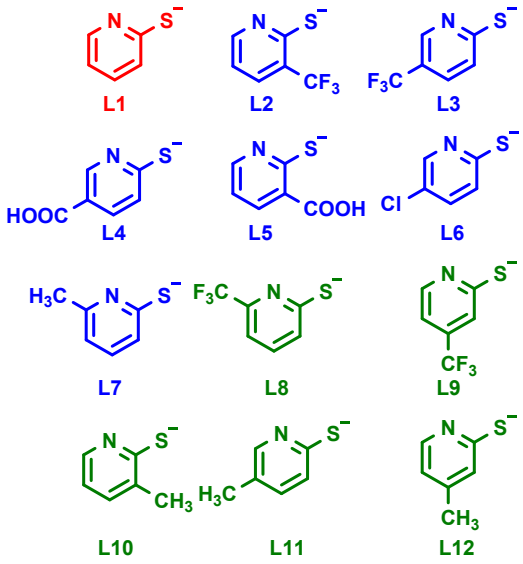

Scheme 1. Pyridinethiolate (PyS-) ligands used to model the family of **[Ni(PyS)$_3$]$^-$** catalysts: The unsubstituted ligand (L1, red); The homoleptic complexes containing ligands L2–L7 (blue) have been investigated both experimentally and computationally;[35,36] the complexes containing ligands L8–L12 (green) have been studied only computationally.

Methods

Density Functional Theory (DFT) Studies: The quantum chemistry package Gaussian 09 suite of programs was used to perform all of the calculations in this report.[45] The geometries of the starting catalyst, **1**$^-$ were optimized in both *singlet* and *triplet* spin states at three different DFT level of theories namely, B3LYP, B3P86, M11-L with 6-311+G(2df,2pd) basis sets in polarized continuum (PCM) water solvation model. The *triplet* configuration of the starting catalyst was chosen by comparing the single-point energies to the singlet states at all the DFT level of theories (Supporting Information, Table S1).[35] The B3P86 functional was chosen for the subsequent calculations, as it best described the geometries of the starting catalysts with the most negative single-point energies for all of the catalysts reported herein. The isomers of protonated intermediates, **1-H**, were modeled with B3P86/6-311+G(2df,2pd) at a *triplet* spin state employing both water and acetonitrile continuum solvation models, while the isomers of reduced intermediates, **1-H**$^-$, were modeled at *doublet* spin state utilizing the same method in both water and acetonitrile implicit solvent models. The frequency calculations were performed on the stationary points and resulted in no imaginary frequencies. The Gibbs energies (*G*) for each intermediate were obtained using the sum of thermal and electronic energies from the thermochemistry calculation using normal mode analyses. The free energy change (ΔG^0_{rxn}) for all the reactions were calculated using *Hess's law* of constant heat summation.

Calculated pK_a Values: The complexes were protonated at the three different N atoms separately, creating the protonated isomers. The geometry of each isomer was optimized, and the pK_a of the individual protonated isomers were calculated (**eqn. 1**).

$$pK_a = -\frac{\Delta G^0}{RTln10} \quad (1)$$

Here, ΔG^0 is the free energy change for reaction described by **eqn. 2**, *R* is the universal gas constant and *T* is the absolute temperature of the system (*298.15 K)*. For the following acid-base reaction described by **eqn. 2**, the free energy change (ΔG^0_{rxn}) of reaction is calculated as follows (**eqn. 3**):

$$1^- + H^+ \rightarrow 1-H \quad (2)$$

$$\Delta G^0_{rxn} = G_{1-H} - (G_{1^-} + G_{H^+}) \quad (3)$$

The free energy change for this acid-base reaction was calculated using the parametric value of *-264 kcal/mol the energy* for a water solvated proton (G_{H^+}) that includes translation entropy and solvation free energy.[16,46–48]

Calculated E^0 Values: Reduction potential values (E^0) were calculated for the reduction steps for all the protonated isomers. The ΔG^0 for the *isodesmic* reaction (**eqn. 4**) was used to obtain the E^0 of the reduction reactions employing **eqn. 5**, where *F* is Faraday's constant and E^0_{ref} is the experimentally reported E^0 for the conversion of $[Ni(PyS)_3]H$ to $[Ni(PyS)_3]H^-$, *-1.62 V vs.* SCE.[36]

$$[Ni(PyS)_3]H + 1-H^- \rightarrow [Ni(PyS)_3]H^- + 1-H \quad (4)$$

$$E^0 = -\frac{\Delta G^0}{F} + E^0_{ref} \quad (5)$$

Computational pK_a and E^0 values, are compared to previously reported experimental data.[36,35]

Thermodynamic Population Analysis: The relative population (*x*) of each of the isomers for the complexes were calculated using the Boltzmann distribution formula at *298.15 K* and normalized to unity with respect to the most stable isomer, assuming the population was determined only by the thermodynamic stability (**eqn. 6**), where ΔG^0_i is the difference in the free energy of the most stable isomer relative to another isomer, *R* is the universal gas constant, and *T* is the absolute temperature.[49] Based on the population analysis, the weight-averaged pK_a values were calculated for the protonated isomers by taking a weighted sum of the pK_a values for the individual isomers and dividing it by 100.

$$x = \frac{\exp\left(-{}^{\Delta G^0_i}/_{RT}\right)}{\Sigma_i \exp\left(-{}^{\Delta G^0_i}/_{RT}\right)} \times 100 \quad (6)$$

Quantum Theory of Atoms in Molecules Analysis: The intramolecular H-bonds that stabilize the isomers were investigated by the topological analysis of the electron density distribution using Bader's Quantum Theory of Atoms in Molecules (QTAIM).[50,51] Wavefunction files for the AIM analyses were prepared from the optimized structures of the complexes using Gaussian 09 package and further analysed by Multiwfn 3.7 program.[45,52] The bond energies (*BE* in *kcal/mol*) of the intramolecular H-bonds were calculated using **eqn. 7**, where $\rho(r)$ is the electron density at the bond critical point (BCP) corresponding to the H-bonding interaction.[53–55]

$$BE \approx -223.08 * \rho(r) + 0.7423 \quad (7)$$

Results and Discussion

Structure of catalysts: The unsubstituted **[Ni(L1)$_3$]$^-$**, **1$^-$**, adopts a pseudo-octahedral geometry, where the Ni (II) center is coordinated by three bidentate pyridinethiolate (PyS$^-$) ligands. Based on the orientation of the ligands around the metal center, the compound might have two geometrical isomers: facial (*fac*) or meridional (*mer*). X-ray crystallographic studies, supported by computational investigations, reveal **1$^-$** is thermodynamically more stable in the chiral *mer* geometry over the *fac* geometry.[22] Computational modelling of the *mer* isomer of **[Ni(L1)$_3$]$^-$** was performed using three functionals, B3P86, B3LYP, and M11-L using 6-311+G(2df,2pd) basis sets, in both *singlet* and *triplet* spin states. The *triplet* spin state of the catalyst is calculated to be about 0.02 Hartrees more stable over the *singlet* spin state, irrespective of the choice of the functional (Supporting Information, Table S1). This is supported by *paramagnetic broadening* observed in the NMR spectrum of the complex.[22] The lowest single point energy was obtained for the B3P86/6-311+G(2df,2pd) as a *triplet* state in the *mer* geometry which best described the structure of the catalyst. Since the three bidentate PyS$^-$ ligands are oriented in *mer* configuration, the chelation is unsymmetrical resulting in the three chelating pyridyl N atoms, and the thiolate S atoms all being different from one another.

The same methods were followed while modelling the ligand modified **[Ni(PyS)$_3$]$^-$** catalysts. Ligand modification through substituting ED and EW groups on the pyridyl ring shows an interesting effect on the structure of the catalyst. When there is a substitution on the C-6 atom of the aromatic ring, the *fac* isomer becomes preferred, which is observed through structure determination using X-ray crystallography for **[Ni(L7)$_3$]$^-$** and via DFT optimized structures by comparing the single-point energies of both the *fac* and *mer* isomers of the same compound.[22] This is observed computationally when C-6 was substituted with an ED methyl group (CH_3) as well as EW trifluoromethyl group (CF_3), which led us to believe that this phenomenon is solely governed by *steric effects* and not *electronic effects*.[22] In the *fac* form of the catalyst, the three chelating N atoms are equivalent due to an identical chemical environment which they belong to (all are trans to a chelating S). Hence, the chemical behavior of these atoms is identical and the pK_a values are the same. However, substitutions made on either C-3, C-4, or C-5 atom do not alter the *mer* arrangement of the ligands around the metal center seen for the unsubstituted catalyst. Hence, these ligand-modified catalysts also have asymmetrical pyridyl N atoms and will result in isomers upon protonation that will need to be considered while computationally modelling these compounds.

Compound **1$^-$** has been shown to catalyze the conversion of H^+ to H_2 under both photochemical and electrochemical conditions (**Figure 1**).[22,33,35,36] We have previously reported that the catalytic mechanism is initiated by the protonation of one of the three pyridyl N atoms, which forms a penta-coordinated **1-H** intermediate.[35] The next step of the catalytic mechanism is the reduction of **1-H** to **1-H$^-$** intermediate. Computational modelling was performed on **1$^-$**, as well as **1-H** and **1-H$^-$** in order to calculate the thermodynamic parameters (pK_a and E^0) responsible for the catalytic activity. The asymmetric environment around the Ni has not been previously considered, and the unique electronic and geometric environment of each N, form three possible protonation sites for the first step of the catalytic cycle.

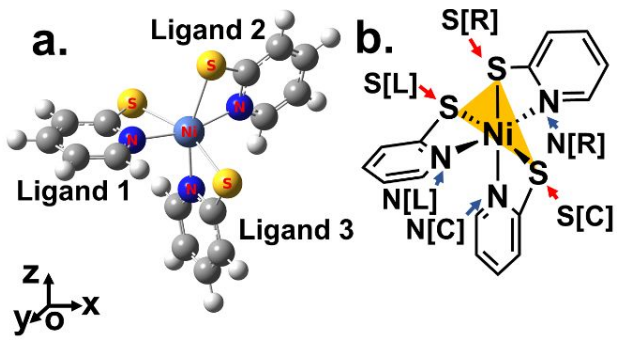

Figure 2. a. Ball and stick representation of the geometry around the Ni-center demonstrating the three different N and S environments, **b.** Nomenclature of the three different pyridyl N atoms. **N[R]** lies right of the plane of S atoms, **N[C]** lies in the plane, and **N[L]** lies to the left of the plane.

Protonation of Ni[(PyS)$_3$]$^-$ catalysts: The three possible protonation sites on different N atoms can be visualized when the molecule is oriented such that the two trans S atoms are placed on the *equatorial plane* of the octahedron, one pointing away and the other into the plane of the page. The third S atom is oriented to the apical position that is along the positive Z-axis, leaving the trans N atom to be on the apical position along the negative Z-axis (considering the Ni center to be the origin). Hence, the bottom apical N atom is connected to the S atom coming into the plane of the page. In this orientation, we can identify the different pyridyl N atoms as N^1, N^2, and N^3, and thiolate S atoms as S^1, S^2, and S^3, where S^1 and N^1 are on the same ligand. N^3 is trans to S^2, and while both N^1 and N^2 are trans to one another, S^1 is trans to S^3 while S^2 is trans to N^3 (**Figure 2a**). Due to the asymmetry of the three PyS^- ligands, the pyridyl N atoms are electronically and geometrically distinct from one another. The first step in the catalytic cycle is protonation of a pyridyl N.[35] Computationally, any one of the pyridyl N atoms can be protonated. Care must be taken when performing computational studies on such structures as appropriate choice of the correct isomer is can alter computational results.

We have established a nomenclature to identify the isomers formed through protonation of each of the N in **1**$^-$. Pyridyl N atoms can be distinguished by drawing an imaginary plane containing S^1, S^2, and S^3 atoms (yellow plane) (**Figure 2b**). If N^3 atom, which belongs to the plane, is oriented down, then N^1 and N^2 atoms will be on the left and right side of that imaginary plane, respectively. For clarity and simplicity, we have identified N^3 as the central (**N[C]**), N^1 as left (**N[L]**), and N^2 as right (**N[R]**) N atom. Thus, if **N[C]** is protonated, we call the generated isomer the **[C]** isomer of **1-H**; therefore, protonation of **N[L]** and **N[R]** results in the formation of **[L]** and **[R]** isomers of **1-H,** respectively (**Figure 3**).

The protonated intermediates, **1-H** were modeled by optimizing structures formed by separately dechelating each of the *three* pyridyl N atoms (**N[C]**, **N[L]**, and **N[R]**) and protonating them. This generated different geometric isomers of **1-H** that were studied using QTAIM-based topology analyses. This revealed that the proton that is attached to the pyridyl N atom can form an intramolecular H-bonding interaction with a S atom from either of the two adjacent PyS^- ligands. For example, after protonating **N[C]**, the newly introduced proton can participate in an intramolecular H-bonding with either **S[L]** or **S[R]** (**N[C]-H…S[L]** or **N[C]-H…S[R]**). Protonation of **N[L]** shows similar interaction with either **S[C]** or **S[R]** (**N[L]-H…S[C]** or **N[L]-H…S[R]**) and protonation of **N[R]** leads to the possibilities of two interactions, either with **S[C]** or **S[L]** (**N[R]-H…S[C]** or **N[R]-H…S[L]**).

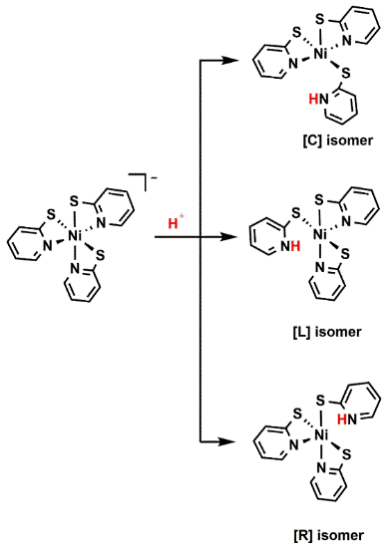

Figure 3. Formation of isomers upon protonation of the different pyridyl N atoms without considering the intramolecular hydrogen bonding between the introduced proton on the pyridyl N atom and adjacent thiolate S atoms.

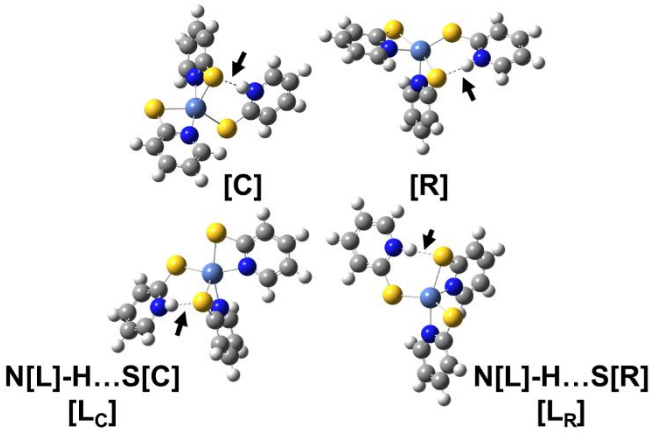

Figure 4. Topology maps represented by ball and stick models of **[C]**, **[L$_C$]**, **[L$_R$]**, and **[R]** (from left to right) isomer of **[Ni(L$_1$)$_3$H]** where blue, grey, yellow, white, and indigo balls represent N, C, S, H and Ni atoms, respectively. Black arrows point toward the intramolecular N-H…S H-bonding interactions.

This leads to the possibility of formation of *six* protonated complexes: **N[C]-H…S[L]** or **[C$_L$]**; **N[C]-H…S[R]** or **[C$_R$]**; **N[L]-H…S[C]** or **[L$_C$]**; **N[L]-H…S[R]** or **[L$_R$]**; **N[R]-H…S[C]** or **[R$_C$]**; **N[R]-H…S[L]** or **[R$_L$]**. However, topology analyses assisted by DFT calculations reveal that **[C$_L$]** and **[C$_R$]**, and **[R$_C$]** and **[R$_L$]** respectively, are the same compound with identical thermodynamic stabilities and properties, collectively referred to as the **[C]** isomer of **1-H**, and the **[R]** isomer of **1-H**, but **[L$_C$]** and **[L$_R$]** optimize to distinct compounds which reduces the number of isomers formed due to the protonation of **1**$^-$, to *four*: **[C]**, **[L$_C$]**, **[L$_R$]**, and **[R]** (**Figure 4**).

The isomers have different thermodynamic stabilities, and hence calculated pK_a values (**Table 1**). For example, considering the unsubstituted **[Ni(L1)$_3$]**$^-$, the calculated pK_a's of **[C]**, **[L$_C$]**, **[L$_R$]**, and **[R]** isomers are 11.4, 11.1, 12.2, and 12.4 respectively (**Table 1**). The **[R]** isomer is calculated to be 1.4 *kcal/mol*, 1.9 *kcal/mol*, and 0.4 *kcal/mol* more stable than the **[C]**, **[L$_C$]**, and **[L$_R$]** isomers,

Table 1. The calculated pK_a for each isomer is presented with the thermodynamic Boltzmann distribution of the isomers at room temperature and the experimental pK_a value.[33,36]

Group	Complex	Calculated pK_a in implicit water solvent model (%Distribution)				Weight averaged pK_a	Experimental pK_a
		[C]	**[L_C]**	**[L_R]**	**[R]**		
-	$[Ni(L1)_3H]$	11.4 (5.27)	11.1 (2.51)	12.2 31.93)	12.4 (60.30)	12.3	12.1
3-CF_3	$[Ni(L2)_3H]$	6.7 (1.52)	6.3 (0.58)	7.0 (3.19)	8.5 (94.70)	8.4	8.3
5-CF_3	$[Ni(L3)_3H]$	6.7 (1.12)	6.7 (1.12)	7.3 (5.38)	8.6 (92.37)	8.5	7.4
6-S-3-COOH	$[Ni(L4)_3H]$	12.1 (2.88)	11.8 (1.37)	12.7 (10.16)	13.6 (85.59)	13.5	10.3
2-S-3-COOH	$[Ni(L5)_3H]$	-4.6 (5.45)	-5.2 (1.23)	-3.9 (24.01)	-3.5 (69.30)	-3.7	8.6
5-Cl	$[Ni(L6)_3H]$	8.2 (4.59)	8.0 (3.00)	8.9 (20.23)	9.4 (72.18)	9.2	7.6
4-CF_3	$[Ni(L9)_3H]$	6.9 (1.36)	7.6 (8.25)	8.3 (40.42)	8.4 (49.97)	8.3	-
3-CH_3	$[Ni(L10)_3H]$	12.0 (9.15)	12.2 (13.99)	12.3 (21.37)	12.7 (55.48)	12.5	-
5-CH_3	$[Ni(L11)_3H]$	12.3 (4.08)	12.0 (1.94)	13.3 (42.03)	13.4 (51.95)	13.3	-
4-CH_3	$[Ni(L12)_3H]$	12.0 (4.52)	12.0 (2.79)	12.7 (13.69)	13.2 (79.00)	13.0	-

respectively. To compare these values to the experimental pK_a value that is reported to be 12.1[33] we could choose the most stable isomer (pK_a 12.4), or attempt to consider all isomers. Calculation of the Boltzmann's distribution on the computationally modeled structures reveals that at room temperature isomer **[R]** would have a 60% contribution, **[C]** has 5%, **[L_C]**, and **[L_R]** have 2% and 32% contribution, respectively (**Table 1**). The weight-averaged calculated pK_a value of the individual isomers is 12.3. The choice of how to correlate computational data to experimental values will be system specific, however this highlights the importance of carefully considering all possible structures in the computational investigation.

Isomers of the protonated intermediate also exist for the complexes with modified ligands. For example, when the PyS^- ligand is modified with EW -CF_3 group on C-3 of the pyridyl rings, it forms the **$[Ni(L2)_3]^-$** complex. The experimentally observed pK_a of this compound is 8.3, while the calculated weight-averaged pK_a value is 8.4 for all protonated isomers.[36] It has been observed through DFT calculations that the **[R]** isomer is 1.4 *kcal/mol*, 3.0 *kcal/mol*, and 2.0 *kcal/mol* more stable than **[C]**, **[L_C]**, and **[L_R]** isomers of the protonated intermediates of **$[Ni(L2)_3]^-$** complex, respectively. The thermodynamic population analyses of these protonated isomers show that the contribution from **[R]** isomer is 95% while **[C]**, **[L_C]**, and **[L_R]** forms contribute about 2%, 1%, and 3% towards the equilibrium isomer distribution. When comparing the experimentally observed pK_a value of 5-chloro substituted tris-(pyridinethiolate)nickel(II) complex; **$[Ni(L6)]_3^-$** (7.6) with the weight-averaged calculated pK_a value (9.2), the **[R]** isomer is again the most contributing (72%) followed by **[L_R]** (20%), **[C]** (5%), and **[L_C]** (3%).[36] The trend remains consistent among the catalysts substituted in the 3- or 5- position; the **[R]** isomer is thermodynamically most stable. As mentioned earlier, when the thiopyridine ring is modified with an ED methyl (CH_3) group or EW trifluoromethyl (CF_3) in the C-6 position, the Ni compounds, **$[Ni(L7)_3]^-$**, and **$[Ni(L8)_3]^-$**, prefer the *fac* geometry rather than the *mer* form as confirmed by both X-ray crystallography and DFT studies (Supporting Information Table S2).[22] This observation hints that structural effects from substitutions at the C-6 position of the ligand is purely guided by *steric effects*. In the corresponding *fac* isomer, all the pyridyl N atoms are identical so there is no isomer formation upon protonation, hence not included further in this study.

Most of the calculated pK_a's are within the range of the systematic computational error reported error using B3P86 level of theory of 2.6 pK_a units.[56] However, compounds **$[Ni(L4)_3]^-$** and **$[Ni(L5)_3]^-$** have computed values outside of this error range, when compared to the experimentally observed values. The calculated structures show close H-O (from the -COOH group) distances, and as we will discuss below, the protonated structures are stabilized by several H-bonds. The pK_a-lowering effect of the stabilizing interaction seen in the computational studies is not observed in the experimentally measured values possibly due to solvent interactions.

Electron donating groups are added to make the catalyst easier to protonate and thus able to operate under more basic conditions. The calculated pK_a values, either taking the weighted average, or considering the most stable isomer show the expected trend (excluding the -COOH derivatives). It also shows position of the substituent is not as important as the electron donating or withdrawing character.

Isomer stability: To quantify the role of intramolecular H-bonding on isomer formation, we used topology analyses based on QTAIM. Originally, we hypothesized that the thiolate S atom would be a better trans-directing ligand than the pyridyl N atom, due to the higher π-acidic character, a weaker N-Ni bond would result for the N trans to the S, resulting in the highest pK_a for the **[C]** isomer. The calculated N-Ni bond lengths support this theory with the **N[C]-Ni** bond being consistently 0.02 Å longer than both the **N[L]-Ni** and **N[R]-Ni** bonds as observed in the crystal structure data (Supporting Information, Table S3 and S4). If this were the main contributor to the thermodynamics of the protonated isomer, the protonation would always take place on the **N[C]** atom as it is the only N atom *trans* to a S atom. However, computations show that the **[C]** isomer is the least thermodynamically favored for all of the protonated derivatives (**Table 1**). Thus, we performed QTAIM based topology analysis to investigate additional factors controlling basicity of the different pyridyl N atoms.

The thermodynamic stability for each of the isomers of the **1-H** intermediates is different (**Table 1**). QTAIM reveals that, after protonation of **1**$^-$, the newly introduced H^+ attached to the pyridyl N atom forms a H-bond with one of the chelating S atoms from the adjacent PyS^- ligands resulting in a distorted square pyramidal structure (**Figure 4**, Supporting Information, Figure S1). We

calculated the energy for these intramolecular H-bonding interactions (**Table 2**), and found the energy is directly related to the thermodynamic stability of the protonated intermediates, *i.e*., the higher the energy of the H-bond, the higher is the relative population of the isomer. Intramolecular H-bonding overcomes the thermodynamic *trans effect* in most cases. It is for this reason, we hypothesize that the formation of a stronger intramolecular H-bond is the key parameter for the protonation of a specific pyridyl N atom and not the *trans effect* imparted by the thiolate S atoms.

Table 2. Topology analysis of the H-bonds in the **1-H** structures for each isomer and the corresponding H-bond strength.

Complex	Calculated H-bond energies [H (r_{bcp}) *kcal/mol*] in implicit water solvation			
	[C]	**[L_C]**	**[L_R]**	**[R]**
[Ni(L1)$_3$H]	-6.32	-5.99	-7.36	-7.39
[Ni(L2)$_3$H]	-6.28	-5.94	-7.23	-7.19
[Ni(L3)$_3$H]	-6.47	-6.30	-7.34	-7.28
[Ni(L4)$_3$H]	-6.24	-6.27	-7.10	-7.06
[Ni(L5)$_3$H]	-6.42	-5.95	-7.12	-7.12
[Ni(L6)$_3$H]	-6.74	-6.63	-7.60	-7.62
[Ni(L9)$_3$H]	-6.40	-6.30	-7.33	-7.38
[Ni(L10)$_3$H]	-6.12	-6.09	-7.30	-7.23
[Ni(L11)$_3$H]	-6.40	-6.08	-7.42	-7.42
[Ni(L12)$_3$H]	-6.06	-6.06	-7.25	-7.29

The intramolecular H-bonds have energies ranging from -5.95 *kcal/mol* to -7.60 *kcal/mol*. The topology analysis further reveals a bonding interaction between the introduced electron-poor proton and the electron-rich chelating S atoms characterized by the presence of a (3,-1) critical point, or a so-called *bond critical point* (BCP). For example, in the case of **[Ni(L1)$_3$H]**, **[R]** is the most stable protonated isomer with the highest intramolecular H-bond stabilization energy of -7.39 *kcal/mol*, while the least stable **[L_C]** isomer has the lowest stabilization energy of -5.99 *kcal/mol*. The stabilization energy of these intramolecular H-bonds is thus correlated with the stability of the protonated intermediates and the stability of different isomers. But there are some outliers: in some cases, the **[L_R]** isomer is characterized by a higher H-bond energy than the **[R]** isomer (0.0 – 0.5 *kcal/mol*) even though the **[R]** isomers are consistently the highest contributor to the equilibrium geometry of the protonated intermediates, as revealed by the Boltzmann distribution analyses. These inconsistencies can be attributed to the electronic effects of the ligand substituents as well as their positions. These modifications lead to the alteration of the electron density on the chelating thiolate S atoms hence further effects on the strength of the said H-bonds. We speculate that the formation of additional H-bonds explains why we observe negative values for calculated pK_a's in the case of protonated **[Ni(L5)$_3$]$^-$**. Therefore, due to the strong intermolecular H-bonds in the starting structure of the catalyst, it is thermodynamically unfavorable to protonate the **[Ni(L5)$_3$]$^-$** complex. However, under experimental conditions these H-bonds are likely disrupted by solvent interactions.

To further comment on the nature and origin of the intramolecular H-bonds in question, it is well-understood that these interactions are extremely dynamic, and we did not incorporate the effect from intermolecular H-bonding in our modeling of the isomer structures. The experimental verification of these H-bonds through NMR spectroscopic methods is restricted due to the paramagnetic *triplet* spin state of the transition metal, and studying the evolution of the system using molecular dynamics simulation while employing an explicit solvent model is computationally expensive. However, this simplistic model describes the available experimentally observed results and provides logical consistency without further expensive and complicated computational treatment.

Reduction of [Ni(PyS)$_3$H] catalysts: The next step in the catalytic cycle is a reduction of the protonated catalyst. We expected to obtain *four* different isomers of the reduced intermediates (**1-H$^-$**) when we computationally modelled the second step of the catalytic cycle (the reduction of **1-H**). The **[C] 1-H** isomer was expected to reduce to the **[C] 1-H$^-$** isomer, while the **[L_C] 1-H**, **[L_R] 1-H**, and **[R] 1-H** were expected to reduce to **[L_C] 1-H$^-$**, **[L_C] 1-H$^-$**, and **[R] 1-H$^-$** isomers, respectively. Thus, we optimized the structure of each protonated isomer with an extra electron at a *doublet* spin state to model the reduction step of the catalytic cycle employing an implicit solvent model for acetonitrile.

Topological analysis was performed on all possible reduced isomers to examine the intramolecular H-bonds between the H$^+$ introduced in the first step of the catalytic cycle and the thiolate S atoms of the adjacent PyS$^-$ ligands (**Table 3**) (Supporting Information, Figure S2). We calculated the bond energies of these intramolecular H-bonds using QTAIM for the reduced intermediates, as before. In almost all cases, we unexpectedly observed that the most stable isomers form the least stable H-bonds. For example, the **[C]** and **[R]** isomers of reduced **[Ni(L1)$_3$H]$^-$** are shown to have the highest Boltzmann populations of about 44% each, while the **[L_C]**, and **[L_R]** isomers contribute only 8% and 4% towards the overall population distribution, respectively, based on calculated thermodynamic data. On the other hand, QTAIM results suggest that the intramolecular H-bond in the **[C]** and **[R]** isomer is about 0.33 *kcal/mol* and 0.43 *kcal/mol* less stable than the H-bonds in **[L_C]**, and **[L_R]** isomers. Thus, unlike the protonated intermediates, the stability of the reduced compound is not correlated with the H-bond formed from the protonated pyridyl N. These observations led us to examine the bond characteristics of the reduced isomers between the central metal ion and ligand framework. After considering the central bonds of the reduced complexes, we observed that in most cases the penta-coordinated reduced isomers form either square pyramidal (*sq. py.*) or trigonal bipyramidal (t_bp) complexes. More importantly, t_bp intermediates are always formed in pairs, in this case the **[C]** and **[R]** isomers of the reduced complexes, where one form is the enantiomer of the other with the same thermodynamic energy, stability, and thus same extent of intramolecular H-bonding between the H atom attached to the pyridyl N and thiolate S atom from the adjacent PyS$^-$ ligand. Thus, after the reduction step the overall number of isomers decreases.

Table 3. Topology analysis of the H-bonds in the **1-H**$^-$ structures for each isomer and the corresponding H-bond strength.

Complex	Calculated H-bond energies [H (r_{bcp}) *kcal/mol*] in implicit acetonitrile solvation			
	[C]	**[L_C]**	**[L_R]**	**[R]**
[Ni(L1)$_3$H]$^-$	-6.06	-6.39	-6.49	-6.06
[Ni(L2)$_3$H]$^-$	-6.08	-6.25	-6.59	-5.90
[Ni(L3)$_3$H]$^-$	-6.23	-6.43	-6.71	-6.26
[Ni(L4)$_3$H]$^-$	-5.96	-6.23	-6.47	-5.96
[Ni(L5)$_3$H]$^-$	-5.80	-6.12	-6.54	-5.78
[Ni(L6)$_3$H]$^-$	-6.53	-6.86	-6.98	-6.53
[Ni(L9)$_3$H]$^-$	-6.27	-6.53	-6.75	-6.27
[Ni(L10)$_3$H]$^-$	-5.85	-6.25	-6.41	-5.85
[Ni(L11)$_3$H]$^-$	-6.06	-6.33	-6.43	-6.06
[Ni(L12)$_3$H]$^-$	-5.92	-6.30	-6.35	-5.92

To classify the structures as *sq. py.* or t_bp, we calculated the *structure index parameter*, tau (τ), for the DFT optimized penta-coordinated intermediates as introduced by Addison *et al.* using **eqn. 9** (**Figure 5**).[57,58] This structure index parameter allows for quantification of the extent of *sq. py.* or t_bp geometry. The calculated τ values (**Table 4**) for the reduced isomers further validate the argument of the formation of two different types of structural isomers upon reduction.

$$\tau = \frac{\beta - \alpha}{60} \qquad (9)$$

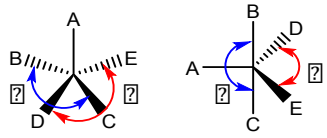

Figure 5. The key angles used to calculate the structure index parameter τ for *sq. py.* and t_bp structures: β and α are the largest basal angles. For an ideal t_bp, β = 180°, α = 120°, and thus τ = 1; ideal *sq. py.*, $\beta = \alpha$ = 180°, so τ = 0.

Table 4. Structure index parameter (τ) for the penta-coordinated reduced intermediates.

	τ [C]	τ [L_C]	τ [L_R]	τ [R]
[Ni(L1)$_3$H]$^-$	0.8	0.2	0.2	0.8
[Ni(L2)$_3$H]$^-$	0.8	0.3	0.4	0.7
[Ni(L3)$_3$H]$^-$	0.8	0.3	0.7	0.7
[Ni(L4)$_3$H]$^-$	0.8	0.2	0.4	0.8
[Ni(L5)$_3$H]$^-$	0.7	0.3	0.6	0.7
[Ni(L6)$_3$H]$^-$	0.8	0.2	0.4	0.8
[Ni(L9)$_3$H]$^-$	0.7	0.3	0.4	0.7
[Ni(L10)$_3$H]$^-$	0.8	0.2	0.3	0.8
[Ni(L11)$_3$H]$^-$	0.8	0.2	0.2	0.8
[Ni(L12)$_3$H]$^-$	0.9	0.2	0.1	0.9

The formation of the two structural isomers also justifies the two contradictory observations obtained from Boltzmann distribution analyses and QTAIM. Since the crystal field stabilization energy of a t_bp is more than the *sq. py.* analogue, the Boltzmann population of the t_bp is higher than the *sq. py.*. However, the degrees of freedom in a *sq. py.* complex is more than that of its t_bp analogue due to its higher symmetry, which allows the former to create a more stable intramolecular H-bond; hence, the extent of stabilization through H-bonding does not correlate with the overall stability of the reduced compounds.

For most of the reduced complexes, two different isomers have equal thermodynamic stabilities and thus the same Boltzmann population. In the case of **[Ni(L1)$_3$H]**$^-$ the **[C]** and **[R]** isomers optimize to the same structure. This means that the reduction of the protonated isomers is not as straightforward as we predicted. For two protonated isomers to form the same reduced isomer, the Ni-N and Ni-S bonds must break and form; one of the ligands has to flip. This type of ligand rearrangement has been experimentally observed in labile complexes with donating S atoms.[59–62]

We calculated the E^0 values for each isomer of all the complexes using the concept of theoretical *isodesmic reactions* as given in **eqn. 5**. Using the experimental E^0 value for the unsubstituted **[Ni(L1)$_3$]**$^-$ of -1.62 V vs SCE[22] as a reference, the computational E^0 values for each isomer of each catalyst was calculated. The reference reaction accounts for solvent, electrode effects, and systematic computational errors. The reported accuracy of calculated E^0 values using an *isodesmic reaction* is *ca.* 0.1 V. We do not see a reasonable correlation between calculated and experimental E^0 values although the calculated trends match what we would expect for the substitutions. For example, the experimentally reported reduction potential for [Ni(L2)$_3$H]$^-$ is -1.26 V vs SCE,[36] compared to the calculated values of -1.41 to -1.49 V vs SCE. We do not currently have a good explanation as to why computed and measured E^0 values are inconsistent. The use of *isodesmic reactions* heavily relies on intermolecular electron transfer between like species and does not account for the bond breaking and new bond formation. Structural changes upon reduction was observed in the optimization that suggests fluxional behavior of the catalyst may result in bond making and breaking which would account for the poor correlation.

Table 5. The calculated E^0 values for each isomer are presented with the thermodynamic Boltzmann distribution of the isomers at room temperature and the experimental E^0 values.[36]

Group	Complex	Calculated Reduction Potential (V vs. SCE) in acetonitrile solvent model (% Distribution)			
		[C]	**[L_C]**	**[L_R]**	**[R]**
-	[Ni(L1)$_3$H]$^-$	(44.29)	(8.39)	(3.72)	(43.59)
3-CF$_3$	[Ni(L2)$_3$H]$^-$	-1.44 (49.02)	-1.44 (7.12)	-1.41 (5.77)	-1.49 (38.09)
5-CF$_3$	[Ni(L3)$_3$H]$^-$	-1.40 (23.57)	-1.41 (5.45)	-1.37 (5.22)	-1.41 (65.76)
6-S-3-COOH	[Ni(L4)$_3$H]$^-$	-1.38 (47.93)	-1.44 (0.99)	-1.37 (4.11)	-1.40 (46.97)
2-S-3-COOH	[Ni(L5)$_3$H]$^-$	-1.57 (8.53)	-1.59 (0.38)	-1.55 (1.82)	-1.51 (89.28)
5-Cl	[Ni(L6)$_3$H]$^-$	-1.48 (46.89)	-1.59 (0.18)	-1.47 (5.99)	-1.49 (46.94)
4-CF$_3$	[Ni(L9)$_3$H]$^-$	-1.70 (38.37)	-1.72 (11.07)	-1.65 (12.60)	-1.69 (37.97)
3-CH$_3$	[Ni(L10)$_3$H]$^-$	-1.70 (38.37)	-1.72 (11.07)	-1.65 (12.60)	-1.69 (37.97)
5-CH$_3$	[Ni(L11)$_3$H]$^-$	-1.65 (45.07)	-1.65 (8.54)	-1.68 (1.70)	-1.65 (44.69)

4-CH$_3$	[Ni(L12)$_3$H]$^-$	-1.67 (38.03)	-1.67 (15.78)	-1.66 (4.92)	-1.69 (41.27)

Furthermore, since the use of *isodesmic reactions* calculates E^0 by the relative difference in theoretically obtained Gibbs energy values for two similar systems, the choice of the isomers in the reaction will affect the results. Although we speculate that the measured E^0 values results from reduction of the most stable protonated isomer (**Table 3**), we cannot be certain which reduced product is ultimately formed. The uncertainty regarding the structure of the final reduced compound is exacerbated by the possibility that isomerization to a thermodynamically more stable compound could occur either before or after the reduction step. However, the computational E^0 values track well with our original expectation of ED groups will make the E^0 values more negative while EW groups will make the E^0 values less negative when comparing with the experimental E^0 value of **[Ni(L1)$_3$H]/ [Ni(L1)$_3$H]$^-$** couple, -1.62 *V vs SCE*.

Conclusions

This work identifies the impact of electronic and geometric ligand features on the basicity of proton reduction catalysts through an exploration of structural isomers formed by protonation of **[Ni(PyS)$_3$]$^-$** type catalysts. The octahedral meridional geometry of the catalyst results in the formation of geometric isomers upon protonation. The formation of isomers depends on which pyridyl N atom is protonated and also the intramolecular H-bonding network between the proton and the S atom from one of the adjacent PyS$^-$ ligands. This results in differences in the computed pK_a values for each isomer by ~3 pK_a units. The basicity is largely dictated by intramolecular H-bonding with neighboring ligands, which is reminiscent of H-bonding effects observed in proteins and other supramolecular structures. In the first reduction step of the proposed catalytic cycle, the catalysts optimize to either a *sq. py.* or t_bp geometry, often with two of the isomers optimizing to the same energy and structure. The t_bp geometry rather than the intramolecular H-bond strength was found to determine the most stable reduced isomer. Combining these findings with previously published investigations we have updated proposed catalytic cycle to reflect the most thermodynamically stable structures (**Figure 6**).[35]

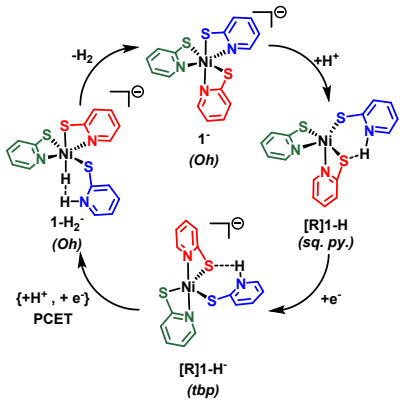

Figure 6. Updated catalytic cycle that depicts the thermodynamically most stable isomers for each step in the proposed mechanism.

This work demonstrates the importance of considering structural isomers when computationally modelling catalytic cycles. The unexpected H-bonding in these structures drastically influences the calculated and measured pK_a values of homogeneous metal catalysts by orders of magnitude which is under-estimated by the simple electronic substitutions. The use of intramolecular H-bonding strength as a descriptor of acidity or basicity (pK_a) is often neglected in small-molecular transition metal catalysis. This report also shows that the extent of H-bonding can possibly overcome the thermodynamic *trans effect*, which is of great interest in the field of catalyst design and reactivity. This demonstrates the importance of carefully considering all electronic and structural modifications aimed at tuning the catalytic activity.

Author Contributions

The Manuscript was written through contributions of all authors. All authors have given approval to the final version of the manuscript.

Conflicts of interest

There are no conflicts to declare.

Acknowledgements

We would like to thank Portland State University, Faculty Enhancement Award for funding this project. The calculations were done on the high-performance computing cluster at Portland State University which was purchased in part with the funds from National Science Foundation (grant DMS 1624776).

References

1 N. S. Lewis, *MRS Bull.*, 2007, **32**, 808–820.
2 R. Eisenberg, H. B. Gray and G. W. Crabtree, *Proc. Natl. Acad. Sci.*, 2019, 1–7.
3 E. S. Rountree, B. D. Mccarthy and J. L. Dempsey, *Inorg. Chem.*, 2019, **58**, 6647–6658.
4 B. D. Mccarthy and J. L. Dempsey, *Inorg. Chem.*, 2017, **56**, 1225–1231.
5 A. Zarkadoulas, M. J. Field, V. Artero and C. A. Mitsopoulou, *ChemCatChem*, 2017, **9**, 2308–2317.
6 M. Drosou, A. Zarkadoulas, K. Bethanis and C. A. Mitsopoulou, *J. Coord. Chem.*, 2021, **74**, 1425–1442.
7 M. Drosou, F. Kamatsos and C. A. Mitsopoulou, *Inorg. Chem. Front.*, 2019, **7**, 37–71.
8 L. Dai, S.; Funk, V. Sautner, M. Paulikat, J. Uranga, R. Mata and K. Tittmann, *Nature*, 2019, **573**, 609–613.
9 P. Gilli, L. Pretto, V. Bertolasi and G. Gilli, *Acc. Chem. Res.*, 2009, **42**, 33–44.
10 A. Warshel, A. Papazyan and P. A. Kollman, *Science*, 1995, **269**, 102–106.
11 W. R. Forsyth, J. M. Antosiewicz and A. D. Robertson, *Proteins Struct. Funct. Genet.*, 2002, **48**, 388–403.
12 S. Cherdo, S. El Ghachtouli, M. Sircoglou, F. Brisset, M. Orio and A. Aukauloo, *Chem. Commun.*, 2014, **50**, 13514–13516.
13 B. Mondal, K. Sengupta, A. Rana, A. Mahammed, M. Botoshansky, S. G. Dey, Z. Gross and A. Dey, *Inorg. Chem.*, 2013, **52**, 3381–3387.
14 C. J. Cramer and D. G. Truhlar, *Phys. Chem. Chem. Phys.*, 2009, **11**, 10757–10816.
15 S. Hammes-Schiffer, *Acc. Chem. Res.*, 2017, **50**, 561–566.
16 B. H. Solis and S. Hammes-Schiffer, *Inorg. Chem.*, 2014, **53**,

6427–6443.
17 C. W. Anson, S. Ghosh, S. Hammes-Schiffer and S. S. Stahl, *J. Am. Chem. Soc.*, 2016, **138**, 4186–4193.
18 H. Ryu, J. Park, H. K. Kim, J. Y. Park, S. T. Kim and M. H. Baik, *Organometallics*, 2018, **37**, 3228–3239.
19 D. Sun, A. Karippara Harshan, J. Pécaut, S. Hammes-Schiffer, C. Costentin and V. Artero, *ChemElectroChem*, 2021, **8**, 2671–2679.
20 W. D. Guerra, E. Odella, M. Secor, J. J. Goings, M. N. Urrutia, B. L. Wadsworth, M. Gervaldo, L. E. Sereno, T. A. Moore, G. F. Moore, S. Hammes-Schiffer and A. L. Moore, *J. Am. Chem. Soc.*, 2020, **142**, 21842–21851.
21 P. Du and R. Eisenberg, *Energy Environ. Sci.*, 2012, **5**, 6012–6021.
22 Z. Han, L. Shen, W. W. Brennessel, P. L. Holland and R. Eisenberg, *J. Am. Chem. Soc.*, 2013, **135**, 14659–14669.
23 D. Hong, Y. Tsukakoshi, H. Kotani, T. Ishizuka, K. Ohkubo, Y. Shiota, K. Yoshizawa, S. Fukuzumi and T. Kojima, *Inorg. Chem.*, 2018, **57**, 7180–7190.
24 S. Inoue, M. Mitsuhashi, T. Ono, Y. N. Yan, Y. Kataoka, M. Handa and T. Kawamoto, *Inorg. Chem.*, 2017, **56**, 12129–12138.
25 F. Kamatsos, M. Drosou and C. A. Mitsopoulou, *Int. J. Hydrogen Energy*, 2021, **46**, 19705–19716.
26 N. A. Race, W. Zhang, M. E. Screen, B. A. Barden and W. R. McNamara, *Chem. Commun.*, 2018, **54**, 3290–3293.
27 A. Das, Z. Han, W. W. Brennessel, P. L. Holland and R. Eisenberg, *ACS Catal.*, 2015, **5**, 1397–1406.
28 Z. Han and R. Eisenberg, *Acc. Chem. Res.*, 2014, **47**, 2537–44.
29 T. L. James, L. Cai, M. C. Muetterties and R. H. Holm, *Inorg. Chem.*, 1996, **35**, 4148–4161.
30 Z. Han, F. Qiu, R. Eisenberg, P. L. Holland and T. D. Krauss, *Science (80-.).*, 2012, **338**, 1321–4.
31 M. P. McLaughlin, T. M. McCormick, R. Eisenberg and P. L. Holland, *Chem. Commun.*, 2011, **47**, 7989–91.
32 P. A. Jacques, V. Artero, J. Pecaut and M. Fontecave, *Proc. Natl. Acad. Sci.*, 2009, **106**, 20627–20632.
33 Z. Han, W. R. McNamara, M.-S. Eum, P. L. Holland and R. Eisenberg, *Angew. Chem. Int. Ed. Engl.*, 2012, **51**, 1667–70.
34 C. C. L. McCrory, C. Uyeda and J. C. Peters, *J. Am. Chem. Soc.*, 2012, **134**, 3164–3170.
35 C. N. Virca and T. M. McCormick, *Dalt. Trans.*, 2015, **44**, 14333–14340.
36 C. N. Virca, J. R. Lohmolder, J. B. Tsang, M. M. Davis and T. M. McCormick, *J. Phys. Chem. A*, 2018, **122**, 3057–3065.
37 A. T. Clark, K. Smith, R. Muhandiram, S. P. Edmondson and J. W. Shriver, *J. Mol. Biol.*, 2007, **372**, 992–1008.
38 D. Bashford and M. Karplus, *Biochemistry*, 1990, **29**, 10219–10225.
39 D. G. Isom, C. A. Castañeda, B. R. Cannon and B. García-moreno E, *Proc. Natl. Acad. Sci.*, 2011, **108**, 5260–5265.
40 C. Han, J. Song, T. Chan, C. Pruett and S. Han, *Biophys. J.*, 2020, **118**, 1838–1849.
41 A. Shokri, A. Abedin, A. Fattahi and S. R. Kass, *J. Am. Chem. Soc.*, 2012, **134**, 10646–10650.
42 A. Shokri, X. Wang and S. R. Kass, *J. Am. Chem. Soc.*, 2013, **135**, 9525–9530.
43 A. Kochem, M. O'Hagan, E. S. Wiedner and M. Van Gastel, *Chem. - A Eur. J.*, 2015, **21**, 10338–10347.
44 P. Jain, R. K. Shukla, S. Pal and V. Avasare, *Catal. Sci. Technol.*, 2020, **10**, 1747–1760.
45 D. J. Frisch, M. J.; Trucks, G. W.; Schlegel, H. B.; Scuseria, G. E.; Robb, M. A.; Cheeseman, J. R.; Scalmani, G.; Barone, V.; Mennucci, B.; Petersson, G. A.; Nakatsuji, H.; Caricato, M.; Li, X.; Hratchian, H. P.; Izmaylov, A. F.; Bloino, J.; Zheng, G.; Sonnenb, *Gaussian 09*, Gaussian, Inc., Wallingford CT, Revision D., 2009.
46 A. V. Marenich, J. Ho, M. L. Coote, C. J. Cramer and D. G. Truhlar, *Phys. Chem. Chem. Phys.*, 2014, **16**, 15068–15106.
47 R. Z. Liao and P. E. M. Siegbahn, *ChemSusChem*, 2017, **10**, 4236–4263.
48 D. Himmel, V. Radtke, B. Butschke and I. Krossing, *Angew. Chemie - Int. Ed.*, 2018, **57**, 4386–4411.
49 I. Grzelak and M. Grzelak, Izabela; Orwat, Botosz; Kownacki, Ireneusz; Hoffmann, *J. Mol. Model.*, 2019, **25**, 1–9.
50 R. F. W. Bader, *Chem. Rev.*, 1991, **91**, 893–928.
51 R. F. W. Bader, *Atoms in Molecules : A Quantum Theory*, Oxford University Press: USA, 1994.
52 T. Lu and F. Chen, *J. Comput. Chem.*, 2012, **33**, 580–592.
53 E. Espinosa, E. Molins and C. Lecomte, *Chem. Phys. Lett.*, 1998, **285**, 170–173.
54 M. A. Spackman, *Chem. Phys. Lett.*, 1999, **301**, 425–429.
55 S. Emamian, T. Lu, H. Kruse and H. Emamian, *J. Comput. Chem.*, 2019, **40**, 2868–2881.
56 X. Qi, L. Liu, Y. Fu and Q. Guo, *Organometallics*, 2006, **25**, 5879–5886.
57 A. W. Addison, T. N. Rao, J. Reedijk, J. van Rijn and G. C. Verschoor, *J. Chem. Soc. Dalt. Trans.*, 1984, **3**, 1349–1356.
58 D. C. Crans, M. L. Tarlton and C. C. Mclauchlan, *Eur. J. Inorg. Chem.*, 2014, 4450–4468.
59 J. C. Peters, S. B. Harkins, S. D. Brown and M. W. Day, *Inorg. Chem.*, 2001, **40**, 5083–5091.
60 A. Takaoka, N. P. Mankad and J. C. Peters, *J. Am. Chem. Soc.*, 2011, **133**, 8440–8443.
61 D. L. M. Suess and J. C. Peters, *Organometallics*, 2012, **31**, 5213–5222.
62 D. Sellmann, T. Gottschalk-Gaudig and F. W. Heinemann, *Inorganica Chim. Acta*, 1998, **269**, 63–72.